

# Miller’s instability, microchaos and the short-term evolution of initially nearby orbits

Amina Helmi\* & Facundo Gómez

*Kapteyn Astronomical Institute, University of Groningen, P.O. Box 800, 9700 AV Groningen, The Netherlands*

## ABSTRACT

We study the phase-space behaviour of nearby trajectories in integrable potentials. We show that the separation of nearby orbits initially diverges very fast, mimicking a nearly exponential behaviour, while at late times it grows linearly. This initial exponential phase, known as Miller’s instability, is commonly found in N-body simulations, and has been attributed to short-term (microscopic) N-body chaos. However we show here analytically that the initial divergence is simply due to the shape of an orbit in phase-space. This result confirms previous suspicions that this transient phenomenon is not related to an instability in the sense of non-integrable behaviour in the dynamics of N-body systems.

**Key words:** stellar dynamics – methods: analytical – methods: N-body simulations – galaxies: kinematics and dynamics

## 1 INTRODUCTION

The problem of how exactly galaxies reach their final equilibrium configuration is still unsolved. It is clear that, unlike for gases, two-body collisions between stars in galaxies are not the driving mechanism to reach a relaxed state, since the associated timescales are exceedingly large (Binney & Tremaine 1987). In an attempt to explain the road to equilibrium from a statistical mechanics point of view, Lynden-Bell (1967) introduced the concept of “violent relaxation”. In this context, the relaxation is reached through the effects of a “violently changing” gravitational field. However, the detailed physics of this process also remain to be understood (Arad & Lynden-Bell 2005; Valluri et al. 2007).

Besides the statistical mechanics approach, it is also possible to study the problem of “relaxation” at the level of orbits. In this case, it is useful to introduce the concept of mixing, by which we mean how quickly nearby particle trajectories diverge in (phase-)space as a function of time. In the case of time-independent gravitational potentials it is customary to classify mixing into two types. If the particles move in an integrable potential, nearby orbits will diverge as a power-law in time, e.g. Helmi & White (1999). This process is known as phase-mixing (Binney & Tremaine 1987). However, when the potential admits a certain amount of chaos, there exist regions of phase-space where nearby orbits diverge exponentially,

evidencing an extreme sensitivity to small changes in the initial conditions (Lichtenberg & Lieberman 1983). This process is known as chaotic-mixing (Kandrup & Mahon 1994; Kandrup 1998).

These mixing processes can also take place in a time-dependent gravitational potential, in which case the energies of the particles will not be constant. The degree of “stickiness”, quantified by the time-evolution of the divergence of nearby orbits would then measure the degree of ergodicity of the mixing process. In the case of chaotic mixing, this could lead to a system that does not have much memory of its evolutionary history. The timescales for evolution could be relatively short, and in principle, this process could be important in the path towards equilibrium for galaxies in the Universe (Merritt 2005; Valluri & Merritt 2000).

Since the 1970s N-body simulations have become the standard tool for studies of the formation and dynamics of structures in the Universe. The question of whether they are a faithful representation of the Universe has always attracted significant attention. This is especially true in recent years (Diemand et al. 2004; Binney 2004), particularly with the finding that dark-matter halos have universal density profiles (Navarro et al. 1996; Moore et al. 1999; Weinberg 2001a,b).

One of the first works to focus on how N-body systems evolve was Miller (1964). Using what must have been the very first computers in the world, he simulated a self-consistent system in virial equilibrium of 8 upto 32 particles distributed randomly in a cubic volume. Miller found that the trajectories of neighbouring particles initially diverged exponentially. This initial transient has been con-

\* Email:ahelmi@astro.rug.nl

firmed using numerical experiments with a significantly larger number of particles (Lecar 1968; Kandrup & Smith 1991; Valluri & Merritt 2000; Hemsendorf & Merritt 2002), as well as with various degrees of numerical softening (Kandrup & Sideris 2001). This implies that the initial exponential divergence cannot be purely attributed to the very grainy nature of the gravitational potential in Miller’s experiments. Furthermore, even in high-resolution N-body realizations of well-behaved integrable systems such as the Plummer sphere, nearby orbits experiment a phase of exponential separation at very early times (Kandrup & Sideris 2003). This initial exponential divergence present in N-body simulations is now known as “Miller’s instability”. Understanding this puzzle is the focus of this paper.

That N-body systems would show a certain degree of chaoticity is not necessarily unexpected. However, it seems natural to expect that the larger the number of particles used to represent an otherwise integrable smooth gravitational potential, the more faithful the representation, and hence the lesser the degree of “numerical” chaos (Quinlan & Tremaine 1992). There is now significant evidence that when such a system is represented by a sufficiently large number of particles, it does tend to the behaviour expected from the collisionless Boltzmann equation (Goodman, Heggie & Hut 1993; El-Zant 2002; Kandrup & Sideris 2003; Sideris 2004).

Nevertheless, even in these high-resolution experiments the initial exponential growth phase is present (Kandrup & Smith 1991; Valluri & Merritt 2000; Kandrup & Sideris 2001). Furthermore, there is evidence (Goodman, Heggie & Hut 1993; Hemsendorf & Merritt 2002) that the rate of divergence associated to this phase increases in proportion to the number of particles used. Because Miller’s instability only lasts for a very short timescale this does not imply that the system is (macroscopically) chaotic (Valluri & Merritt 2000). As stated by El-Zant (2002) it is likely that the “mechanism leading to the short e-folding time in point particle systems is physically unimportant”.

So, while the existence of a continuum limit in N-body systems appears to be more or less established for long timescales, on short timescales Miller’s instability remains a puzzle. The physical mechanism responsible for this was hitherto unknown. It seems quite unlikely that collisions between particles could be important on timescales as short as one-tenth of the crossing time of the system, as measured for example by Hemsendorf & Merritt (2002). Microscopic chaos arising from “white-noise” or poor orbit integrations are also unlikely to be important on those timescales, particularly in integrable (well-behaved) potentials.

In this paper, we tackle this paradox by studying the *initial* behaviour of nearby characteristics in an integrable smooth (and analytic) potential. Our aim is to understand how these nearby characteristics diverge on short timescales, and if they do so at nearly exponential rates. As we shall demonstrate below, this is indeed the case. The initial behaviour mimics an exponential divergence, but since the system is fully integrable this is not related to the presence of chaos. This near-exponential behaviour merely reflects the time evolution of an orbit in phase-space. This result shows that there is no need to introduce the concept of microscopic chaos, and confirms previous suspicions that this transient

phenomenon is not related to an instability in the sense of non-integrable behaviour in the dynamics of N-body systems.

In this paper we describe the evolution of nearby orbits in phase-space, and in particular in configuration space, expanding upon a model developed by Helmi & White (1999) (hereafter HW). The details of this formalism are given in Sec. 2. In this Section we focus in detail on the behaviour of nearby orbits in a Plummer potential. In Sec. 3 we summarize our results.

## 2 THE EVOLUTION IN PHASE-SPACE OF NEARBY ORBITS IN INTEGRABLE POTENTIALS

The problem of the phase-space evolution of nearby orbits has many applications. Some of the most recent are related to the evolution of streams formed by the disruption of satellite systems (dwarf galaxies, globular clusters) in an external (Galactic) potential. This is also the basis of the formalism that HW developed, which is based on the conservation of phase-space density. It consists in a mapping from the initial to the final configurations using adiabatic invariants (a schematic flow chart is given in Figure 1).

The basic idea is to map the initial system onto action-angle space, then follow the much simpler evolution in this space, and finally transform back *locally* onto observable coordinates (all these being linear transformations; for details see HW). This method, which uses action-angle variables, is very general and can be applied to any potential that admits regular orbits (Goldstein 1959; Binney & Tremaine 1987). However, if the potential is separable, the implementation is simpler. This includes all spherically symmetric potentials but only few axisymmetric and triaxial cases, such as the general class of Stäckel potentials e.g. Lynden-Bell (1962); De Zeeuw (1985); Dejonghe & De Zeeuw (1988). In this paper we shall only focus on spherical potentials because these are the simplest to model, while at the same time, they evidence a generic behaviour.

Therefore, instead of following the evolution of pairs of nearby orbits as is traditional in N-body systems, we follow the evolution of a distribution function in phase-space. In particular, and for simplicity, we assume this distribution function to be a multivariate Gaussian (in 6-dimensions).

The work presented here exploits and expands in two new directions the HW algorithm. Firstly, we now compute the behaviour of streams in physical space (to be able to determine the evolution of the spatial separation of nearby trajectories). Secondly, we derive explicitly new analytic expressions for this evolution on short timescales.

### 2.1 The evolution of the distribution function

As discussed above, we assume that the initial distribution function of the system is a multivariate Gaussian in  $\varpi = (\mathbf{x}, \mathbf{v})$  coordinates centered on  $\langle \varpi_0 \rangle$  (a given particle or orbit):

$$f(\varpi, t_0) = f_0 \exp \left[ -\frac{1}{2} \Delta_{\varpi,0}^\dagger \sigma_{\varpi,0} \Delta_{\varpi,0} \right] \quad (1)$$

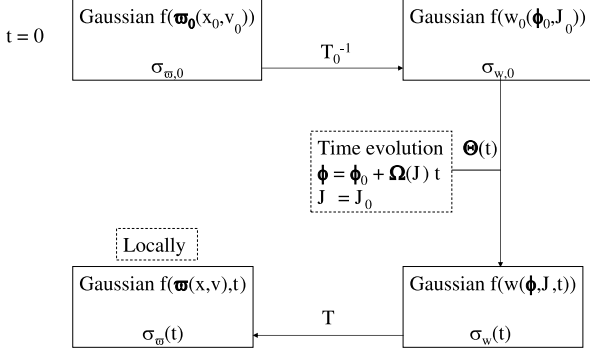


**Figure 1.** Flow chart showing the basic steps of our analytic formalism to measure the evolution of a system in phase-space.

where  $\Delta_{\varpi,0} = \varpi - \langle \varpi_0 \rangle$ , and  $\sigma_{\varpi,0}$  is the variance matrix (the inverse of the covariance matrix) at the initial time:

$$\sigma_{\varpi,0} = \begin{bmatrix} \mathbf{S}_{\mathbf{x},0} & \mathbf{C}_{\mathbf{xv},0} \\ \mathbf{C}_{\mathbf{xv},0} & \sigma_{\mathbf{v},0} \end{bmatrix}. \quad (2)$$

For example, if the variance matrix is diagonal, then  $\mathbf{S}_{\mathbf{x}} = [1/\sigma_{x_i}^2 \delta_{ij}]$  and  $\sigma_{\mathbf{v}} = [1/\sigma_{v_i}^2 \delta_{ij}]$ , and  $\mathbf{C}_{\mathbf{xv}} = \mathbf{0}$ .

A mapping  $\mathbf{T} : \varpi \leftarrow w = (\phi, \mathbf{J})$  will be linear provided the extent of the system in phase-space is small. Its elements are  $T_{ij} = \partial \varpi_i / \partial w_j$  evaluated at  $\langle \varpi \rangle$ . Such a mapping will preserve the form of the distribution function. This will now be a Gaussian in action-angle space, with variance matrix  $\sigma_{w,0} = \mathbf{T}_0^\dagger \sigma_{\varpi,0} \mathbf{T}_0$ .

The dynamical evolution of the system in action-angle coordinates is given by

$$\dot{\phi} = \dot{\phi}_0 + \Omega(\mathbf{J})t, \quad \mathbf{J} = \mathbf{constant}. \quad (3)$$

We may express

$$\Delta_w = \Theta(t) \Delta_{w,0} \quad \text{since} \quad \Delta \phi_{0,i} \sim -\Delta \phi_i - \frac{\partial \Omega_i}{\partial J_j} \Delta J_j t,$$

and where

$$\Theta(t) = \begin{bmatrix} \mathcal{I}_3 & -\Omega' t \\ \mathbf{0} & \mathcal{I}_3 \end{bmatrix}. \quad (4)$$

$\mathcal{I}_3$  here is the identity matrix in 3-D, and  $\Omega'$  represents a  $3 \times 3$  matrix whose elements are  $\partial \Omega_i / \partial J_j$ .

Therefore the distribution function at time  $t$  is

$$f(\mathbf{w}, t) = f_0 \exp \left[ -\frac{1}{2} \Delta_w^\dagger \sigma_w \Delta_w \right], \quad (5)$$

where  $\sigma_w$  is now a function of time

$$\sigma_w = \Theta(t)^\dagger \sigma_{w,0} \Theta(t). \quad (6)$$

Finally, using Eq. (5) we may derive the distribution function in configuration and velocity space at time  $t$ . To this end, we perform a local transformation using the matrix  $\mathbf{T}$ . Since this is done locally, our distribution function is still a multivariate Gaussian. The variance matrix at time  $t$  is

$$\sigma_{\varpi}(t) = (\mathbf{T}_0 \Theta(t) \mathbf{T}^{-1})^\dagger \sigma_{w,0} (\mathbf{T}_0 \Theta(t) \mathbf{T}^{-1}). \quad (7)$$

The variance matrix contains all the information about the properties of the particles on initially nearby orbits. For

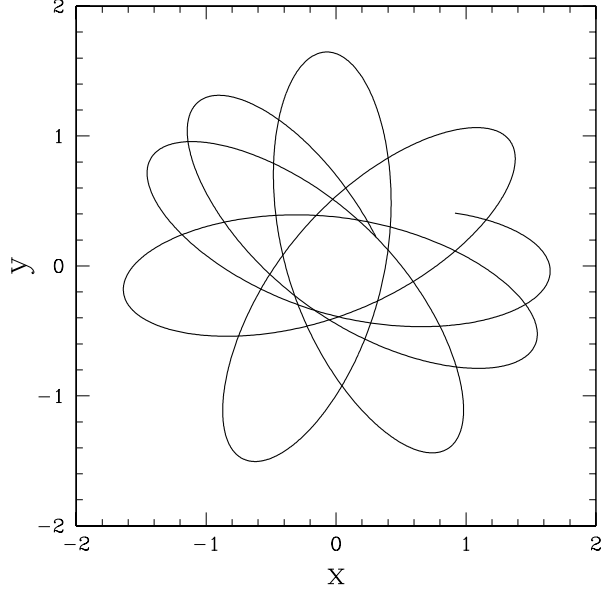


**Figure 2.** Example of an orbit integrated in a Plummer potential.

example, the evolution of the velocity ellipsoid may be derived from the velocity submatrix:  $\sigma_{\mathbf{v}}$ . This submatrix describes the velocity distribution of nearby particles at time  $t$ . The spatial density at a particular location  $\mathbf{x}$  at time  $t$  (which is related to the spatial separation of those particles) is obtained by integrating the distribution function with respect to all velocities:

$$\rho(\mathbf{x}, t) = (2\pi)^3 f_0 \sigma_{v_1} \sigma_{v_2} \sigma_{v_3} \times \exp \left[ -\frac{1}{2} \Delta_{\mathbf{x}}^\dagger \sigma_{\mathbf{x}} \Delta_{\mathbf{x}} \right] \quad (8)$$

where  $\sigma_{v_{i=1,2,3}}$  are the velocity dispersions along the principal components of the velocity ellipsoid. The matrix  $\sigma_{\mathbf{x}}$  is  $3 \times 3$ , and contains all the information concerning the evolution of the particle distribution in configuration space, including their separation, which is ultimately, the quantity that we want to measure.

## 2.2 Example: Evolution in a Plummer potential

This simple spherical gravitational potential has the form

$$\phi(r) = -\frac{GM}{\sqrt{r^2 + b^2}}. \quad (9)$$

Units were so chosen that  $G = M = b = 1$  and the internal energy of the system is  $E = -\frac{3\pi}{64}$ . We define the crossing time of the system  $t_{cr} = R/V$  where  $R = -GM^2/2E$  and  $V^2 = -2E/M$ . For example, for a dwarf galaxy size system with  $b = 0.5$  kpc and  $M = 10^7 M_\odot$ , then  $t_{cr} \sim 0.33$  Gyr.

We assume that the initial 6D variance matrix  $\sigma_w^0$  is diagonal (see Eq. 2), with  $\mathbf{S}_{\mathbf{x},0} = [1/\sigma_x^2 \delta_{ij}]$  and  $\sigma_{\mathbf{v},0} = [1/\sigma_v^2 \delta_{ij}]$ , and where  $\sigma_x = 10^{-5}$  and  $\sigma_v = 10^{-5}$ . We set the central particle of the system on an orbit whose apocentre is located at  $r_a = 1.635b$ , as shown in Fig. 2.

In Figure 3 we plot the evolution of the velocity dispersions, the spatial density and the dispersions in configuration space as function of time, for the orbit shown in Figure 2. These are computed using the procedure outlined in the previous section.

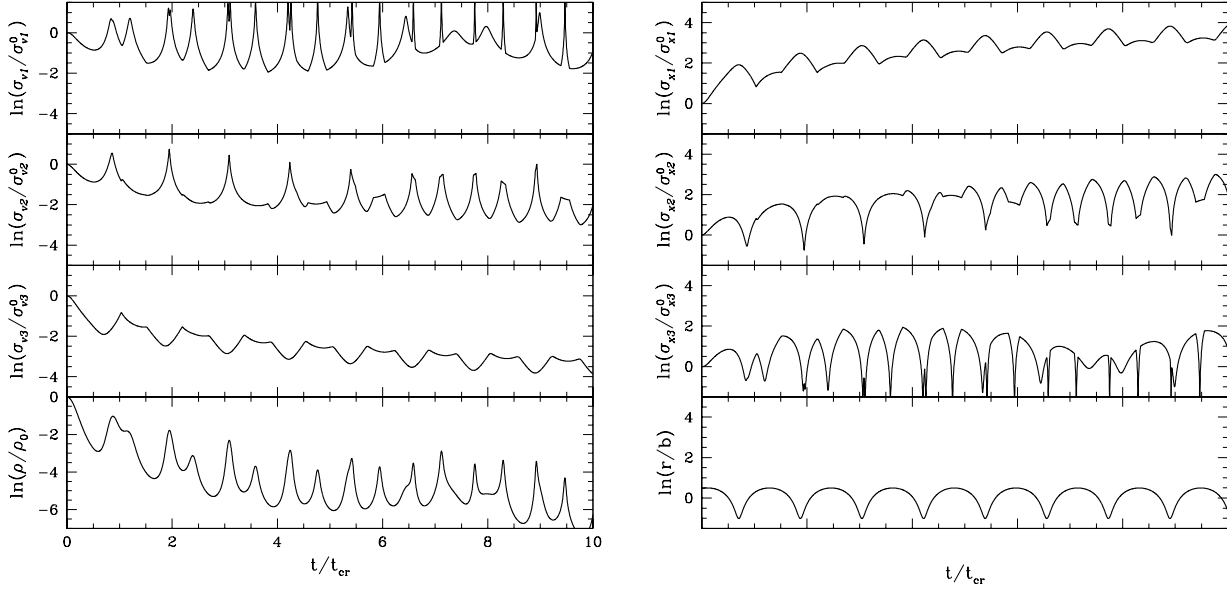


**Figure 3.** Time evolution of the velocity dispersions (top three panels on the left), spatial density (bottom left panel) and dispersions in configuration space (top three panels on the right), for a system moving in a Plummer potential on the orbit shown in Figure 2. The periodicity observed is related to the radial (and angular) orbital oscillations, as shown in the bottom panel on the right.

Figure 3 shows that in the case of spherical potentials, only two of the velocity dispersions decrease in time, while the third one remains on average constant (it corresponds to the direction perpendicular to the plane of motion). These results imply that the configuration-space dispersions will increase in time, as a consequence of Liouville’s theorem (i.e. the conservation of phase-space density). This can also be seen from  $dM \sim \rho \times \sigma_{x_1} \sigma_{x_2} \sigma_{x_3} = cst$ .

The form of the dispersions in velocity and in configuration space has been derived explicitly in the Appendix. There we work in a reference frame that coincides with the plane of motion (this is of course possible for a spherical potential). In this new frame only two coordinates and two velocities are required to specify completely the state of system. In this case, the spatial density

$$\rho \propto \sigma_{v_1} \sigma_{v_2} = (\lambda_{v_1} \lambda_{v_2})^{-1/2}, \quad (10)$$

where  $\lambda_v$  denotes the eigenvalues of the velocity submatrix  $\sigma_v$ , and for which the following relation holds

$$\lambda_{v_1} \lambda_{v_2} = \frac{r^2 p_r^2}{\Omega_r^2} (\alpha_4 t^4 + \alpha_3 t^3 + \alpha_2 t^2 + \alpha_1 t + \alpha_0). \quad (11)$$

The coefficients  $\alpha_i$  depend both on location along the orbit as well as on the initial extent of the system in phase-space (see Eq. A7). The very rapid decrease in the spatial density of the system observed in Fig. 3 can be understood from Eqs. (10) and (11). This decrease implies a rapid separation of the particles (and hence of their orbits). Furthermore, the strong enhancements in the density seen in Fig. 3 take place at the orbital turning points: when  $p_r = 0$  then  $\lambda_{v_1} \times \lambda_{v_2} \rightarrow 0$  and hence  $\rho \rightarrow \infty$ .

In the Appendix (see Eq. A12), we show that the configuration-space dispersions  $\sigma_{x_1} \sigma_{x_2} = \sqrt{\frac{\lambda_{v_1} \lambda_{v_2}}{\det \sigma_w^0}}$ . Close

inspection of Eqs. (11) and (A7), allows us to reach the following conclusions:

- For very short timescales, the term with  $\alpha_0$  dominates. In this case the separation of nearby orbits as measured by  $\sigma_x$  purely reflects the geometry of the orbit in phase space (being heavily weighted by  $r^2 p_r^2$ ).
- The terms with  $\alpha_2$  and  $\alpha_4$  are always positive, implying that these will induce a rapid increase in the  $\lambda_v$ , and hence of the dispersions in configuration space on intermediate timescales.
- The terms with  $\alpha_1$  and  $\alpha_3$  can either be positive or negative, depending on location along the orbit. This (partly) explains the strong oscillatory behaviour observed in Fig. 3.
- On longer timescales, only the term  $\alpha_4 t^4$  is important. This gives rise to the secular behaviour of density which decreases as  $1/t^2$  (as found by HW), and for the dispersions in configuration-space to increase as  $t$ .

### 2.2.1 Relating the dispersion to the separation in configuration space

Our main aim is to study the separation of initially nearby orbits in configuration space. The question is how this separation is related to the dispersions or the variances (i.e. the inverse of the eigenvalues) in the configuration-space matrix  $\sigma_x$ .

We examine three possibilities obtained by performing three different kinds of averages of the configuration-space dispersions:

- the geometric mean:  $\Delta_g = (\sigma_{x_1} \sigma_{x_2} \sigma_{x_3})^{1/3}$ ,
- the arithmetic mean:  $\Delta_a = (\sigma_{x_1} + \sigma_{x_2} + \sigma_{x_3})/3$ ,
- the modulus:  $\Delta_m = \sqrt{\sigma_{x_1}^2 + \sigma_{x_2}^2 + \sigma_{x_3}^2}/3$ .

Figure 4 shows the behaviour of these different averages.

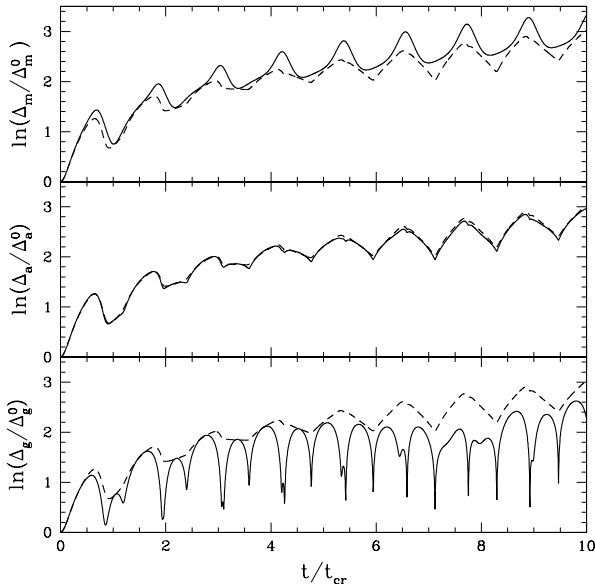


**Figure 4.** Time evolution of three possible averages of the dispersions in configuration-space, as obtained through our formalism. Note the very fast initial growth and the linear behaviour at late times. The dashed curve in each panel represents the average separation  $\langle \Delta_r \rangle$  of 1000 nearby orbits. Note the excellent agreement between  $\langle \Delta_r \rangle$  and  $\Delta_a$  (middle panel).

In all cases, one observes initially a very fast increase in the measured values, while at late times the growth proceeds linearly with time [see also Eqs. (A6) and (A10)].

The question now is how to relate the above defined averages to the separations between two initially nearby orbits. To address this we have generated 1000 orbits with initial conditions distributed according to a Gaussian in configuration space with dispersion  $\sigma_x = 10^{-5}$  and  $\sigma_v = 10^{-5}$  around the orbit shown in Fig. 2. We measure the separation  $\Delta_r = |\mathbf{r}_i - \mathbf{r}_0|$  between this orbit and the 1000 neighbouring trajectories, and derive the average  $\langle \Delta_r \rangle$ . This is plotted as a dashed curve in the panels of Fig. 4. As can be seen, the arithmetic mean  $\Delta_a$  of the configuration-space dispersions computed using the analytic formalism discussed in the previous section provides an excellent measurement of the separation between nearby orbits.

Figure 4 shows that the separation of nearby orbits in smooth integrable potentials exhibits an initial rapid divergence, which is followed by a secular increase which is linear in time. Note that this occurs for a completely integrable system, without any degree of chaos. Therefore we see already that the initial exponential divergence cannot be attributed to any form of chaos whatsoever. It simply reflects the way an orbit evolves in phase-space, as shown in the Appendix.

### 2.2.2 Direct comparison to N-body simulations

The behaviour visible in Figure 4 is strikingly similar to that observed in the N-body simulations shown in Fig. 1 of Valluri & Merritt (2000) and in the frozen N-body realizations of Kandrup & Sideris (2003). To provide the reader with a more direct comparison to our analytic results, we

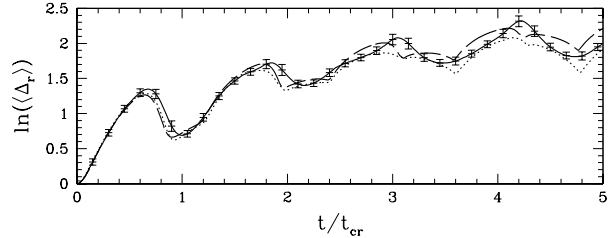


**Figure 5.** Time evolution of the average separation  $\langle \Delta_r \rangle$  of 100 nearby orbits integrated in a frozen N-body realization of the Plummer sphere (solid curve). The error bars correspond to the error on this average. The dashed curve represents the separation of nearby orbits as measured by  $\Delta_a$  using our analytic prescription, while the dotted line represents the same quantity but estimated from the 100 orbits integrated in the N-body realization.

will now analyse the divergence of an ensemble of initially nearby orbits evolved in a potential represented by a finite number of particles.

We have generated a realization of the Plummer sphere, whose density profile is

$$\rho(r) = \frac{3M}{4\pi b^3} \left( 1 + \frac{r^2}{b^2} \right)^{-5/2}, \quad (12)$$

which we have truncated at a radius  $r_t = 12.197b$ , that encloses 99% of its mass. We represent this system with  $N = 128,000$  particles, and use a numerical softening  $\epsilon = 0.025b$  (see e.g. Athanassoula et al. (2000)). Following Kandrup & Sideris (2001) we integrate orbits in this frozen (in time and space) N-body realization. The integration of the orbits was performed using a Runge-Kutta-Fehlberg algorithm of order 4–5.

As in the previous section, we follow the evolution of 100 orbits distributed according to a Gaussian in phase space with initial dispersion  $\sigma_x = 10^{-5}$  and  $\sigma_v = 10^{-5}$  around the orbit shown in Fig. 2. For this ensemble we have measured the time evolution of the average separation  $\langle \Delta_r \rangle$  and of the 6D variance matrix.

The results are shown in Fig. 5. The initial behaviour is very similar, whether derived using our analytic formalism ( $\Delta_a$ , dashed curve) or using the average separation of 100 orbits in the N-body representation of the system ( $\langle \Delta_r \rangle$ , solid curve). The small differences can be attributed to two causes. First of all, the finite sampling of phase-space around the central orbit introduces an error in the average, which is quantified by the error bars shown in this figure. Secondly,  $\langle \Delta_r \rangle$  is not exactly identical to  $\Delta_a$  (see Figure 4). If we compare the quantity  $\Delta_a$  obtained using the 6D variance matrix from the frozen N-body simulation (dotted curve) with that from the analytic formalism (dashed curve), this difference almost disappears. The two curves are virtually indistinguishable over a timescale of a few crossing times.

### 2.2.3 Dependence on initial conditions

It is also interesting to understand how the separation of initially nearby orbits depends on their initial conditions. In particular, how the initial divergence depends on the region of phase-space sampled at short times.

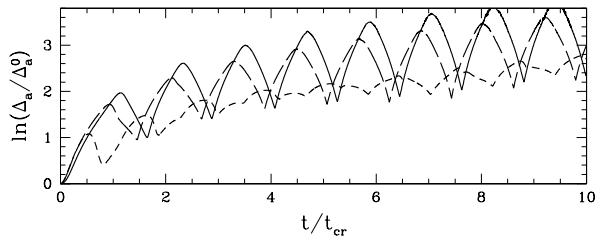


**Figure 6.** Time evolution of the separation of nearby orbits as measured by the arithmetic mean  $\Delta_a$  for the same orbit discussed in previous figures. The sensitivity to initial location along a given orbit is evidenced by the various curves: solid corresponds to initial location at pericentre; short-dashed to apocentre and long-dashed to the average distance between these turning points.

In Figure 6 we plot the time evolution of the arithmetic mean of the three dispersions in configuration space  $\Delta_a$  obtained using our analytic prescription for the orbit shown in Fig. 2. We now plot the behaviour for different starting points along this orbit: apocentre, pericentre and (apocentre + pericentre)/2. We see clearly that the behaviour at short times depends on the initial location along the orbit. The initial divergence is in all cases nearly exponential, but has largest amplitude (it lasts longer) when the integration is started near pericentre.

It is also interesting to study the behaviour of different sets of nearby orbits. Figure 7 shows the evolution for two additional examples. The top panel corresponds to an orbit constrained to move in the inner regions of the system (pericentre  $r_p = 0.62b$  and apocentre  $r_a = 0.88b$ ), while the bottom panel has  $r_p = 1.73b$  and  $r_a = 2.94b$ , and hence it is constrained to the outskirts. Clearly the amplitude of the initial growth phase depends on the regions of phase-space the orbits probe.

Note that, because the quantities shown are normalized to their initial conditions, these results are independent of the initial separation of the orbits (or the values of  $\sigma_{ii}$  in our formalism). This is perhaps, the most characteristic difference between an integrable and a chaotic system. The amplitude (or the rate) of the initial divergence *for a given orbit* is always the same in the integrable case, irrespective of initial separation. To the contrary, in a chaotic system, in the limit of infinitesimal perturbations, the orbits may be trapped near a resonance and cease to be chaotic to become regular. Hence the amplitude of the initial divergence will, in the chaotic case, depend strongly on the initial separation of the orbits.

#### 2.2.4 Miller’s instability and the initial behaviour

The above analysis shows that the initial very rapid divergence of nearby orbits is a generic feature of dynamical systems. It is not only observed in the Plummer potential discussed here, but also in all integrable potentials studied by HW (e.g. Fig. 7 and 9 of their paper).

The initial behaviour is nearly exponential, as shown in Fig. 7 for the orbits discussed so far. The rate of divergence –the equivalent of the “short-term” Lyapunov expo-

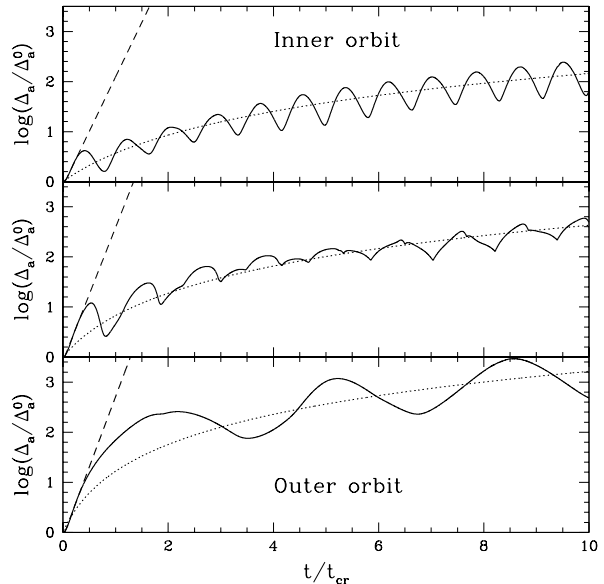


**Figure 7.** Time evolution of the separation of nearby orbits as measured by the arithmetic mean  $\Delta_a$ . The various panels represent orbits probing different regions of the system, all integrated from their apocentres. The dotted curves are exponential fits to the initial (transient) behaviour, while the dashed curves are linear fits to the long-term (secular) behaviour of  $\Delta_a$ .

nent, is  $\chi_e \sim 13.6/t_{cr}$  for the inner orbit,  $\chi_e \sim 16.7/t_{cr}$  and  $\chi_e \sim 17.57/t_{cr}$  for the intermediate and outer orbits, respectively. In all cases, the secular behaviour at late times can be fit by a linear function of time  $\Delta_a = \Delta_{a,0} + t/t_{sec}$ , where the divergence timescale is  $t_{sec} \sim 1.3t_{cr}$ ,  $t_{sec} \sim 0.77t_{cr}$  and  $t_{sec} \sim 0.41t_{cr}$  for the different orbits.

### 3 DISCUSSION

Our analysis shows that the initial nearly-exponential divergence of nearby orbits in N-body systems is not due to chaos. It is present also in integrable smooth potentials, and it reflects a power-law divergence modulated by the shape of an orbit in phase-space.

It is interesting to note that the rates of divergence that we measure using our formalism are in very good agreement with those obtained by Hemsendorf & Merritt (2002) for N-body realizations of the same Plummer sphere. These authors find a characteristic e-folding time of  $t_{cr}/20$  for systems with  $N \sim 10^5$  particles, which is very comparable to the values obtained in Section 2.2.4. They also find a weak dependence on  $N$ , which may also be readily understood within our framework. Such a dependence is induced by the very rapid decrease in the spatial density of the system. If a “relatively” small number of particles is used in a N-body simulation, then the density cannot be mapped properly. For example, to measure a decline in the density of  $10^{-5}$  on a timescale of  $\sim 3t_{cr}$  as observed in Fig. 3, N-body realizations with at least  $10^5$  nearby particles are needed.

Previous works, including Miller (1964) and Kandrup & Sideris (2003) have also noted an oscillatory behaviour in the divergence of nearby orbits. Our

analysis, as well as Figure 3 show that this is due to the modulation produced by the periodicity of a regular orbit in phase-space. It is not, as suggested by Miller (1964), due to the formation of tight binaries in an N-body system. The fact that such behaviour was visible in the various N-body studies presented in the literature, in fact demonstrates that such N-body systems were faithful representations of the true (integrable) system, at least on short timescales. As stated by Kandrup (1998) and Valluri & Merritt (2000), the Lyapunov exponents need to be measured in the limit of infinite time intervals; short-time exponential-like divergences do not imply chaotic behaviour.

## ACKNOWLEDGMENTS

We thank Daniel Carpintero for bringing up this problem to our attention as well as Simon White and Ortwin Gerhard for enlightening discussions. NWO, NOVA and the Kapteyn Institute are gratefully acknowledged for financial support.

## REFERENCES

- Arad, I., & Lynden-Bell, D. 2005, MNRAS, 361, 385  
 Athanassoula E., Fady E., Lambert J. C., & Bosma A. 2000, MNRAS, 314, 475  
 Binney J., 2004, MNRAS, 350, 939  
 Binney J., Tremaine S., 1987, Galactic Dynamics. Princeton University Press, Princeton, NJ  
 De Zeeuw P.T., 1985, MNRAS, 216, 273  
 Dejonghe H. & De Zeeuw P.T., 1988, ApJ, 333, 90  
 Diemand J., Moore B., Stadel J., & Kazantzidis S., 2004, MNRAS, 348, 977  
 El-Zant A., 2002, MNRAS, 331, 23  
 Goldstein H., 1959, Classical Mechanics. Addison-Wesley, Massachusetts  
 Goodman J., Heggie D.C., & Hut P., 1993, ApJ, 415, 715  
 Helmi A. & White S.D.M., 1999, MNRAS, 307, 495  
 Hensendorff M. & Merritt D., 2002, ApJ, 580, 606  
 Kandrup H.E. & Smith H., 1991, ApJ, 374, 255  
 Kandrup H.E. & Mahon M.E., 1994, A&A, 290, 762  
 Kandrup H.E., 1998, MNRAS 301, 960  
 Kandrup H.E. & Sideris I.V., 2001, Phys. Rev. E, 64, 056209  
 Kandrup H.E. & Sideris I.V., 2003, ApJ, 585, 244  
 Lecar M., 1968, Bull. Astron., 3, 91  
 Lichtenberg A.J. & Leiberman M.A., 1983, Regular and Stochastic motion, Springer, New York  
 Lynden-Bell, D. 1962, MNRAS, 124, L95  
 Lynden-Bell, D. 1967, MNRAS, 136, 101  
 Merritt D., 2005, astro-ph/0502169  
 Miller R.H., 1964, ApJ, 140, 250  
 Miller R.H., 1999, Celestial Mechanics and Dynamical Astronomy, 73, 139  
 Moore B., Quinn T., Governato F., Stadel J., & Lake G. 1999, MNRAS, 310, 1147  
 Navarro J.F., Frenk C.S., & White S.D.M. 1996, ApJ, 462, 563  
 Quinlan G.D. & Tremaine S. 1992, MNRAS, 259, 505  
 Sideris I.V. 2004, Celestial Mechanics and Dynamical Astronomy, 90, 149  
 Valluri M. & Merritt D., 2000, in The Chaotic Universe, ed. V.G. Gurzadyan & R. Ruffini (Singapore: World Scientific), 229  
 Valluri M., Vass I.M., Kazantzidis S., Kravtsov A.V., & Bohn C.L., 2007, ApJ, 658, 731  
 Weinberg M., 2001, MNRAS, 328, 311  
 Weinberg M., 2001, MNRAS, 328, 321

**APPENDIX A: MATRICES IN A SPHERICAL POTENTIAL**

For spherical potentials  $\Phi(r)$ , we may choose a system of coordinates that coincides with the plane of motion of the system. In this plane the position of a particle is specified by its angular ( $\psi$ ) and radial ( $r$ ) coordinates. The actions of an orbit in this case are:

$$L = J_\psi = p_\psi, \quad J_r = \frac{1}{\pi} \int_{r_1}^{r_2} dr \frac{1}{r} \sqrt{2[E - \Phi(r)]r^2 - L^2}, \quad (\text{A1})$$

where  $L$  is the total angular momentum of the particle,  $E$  is its energy, and  $r_1$  and  $r_2$  the orbital turning points.

In order to track the evolution of the dispersions of our initial distribution function,  $f(\varpi, t_0)$ , we perform the following sequence of operations. Firstly, we transform from Cartesian coordinates  $\varpi = (\mathbf{x}, \mathbf{v})$  to action angle variables  $w = (\theta, \mathbf{J})$ . The distribution function is then evolved in this space, after which, we transform back to Cartesian coordinates (see Figure 1).

For the sake of simplicity, here we begin with a distribution function already expressed in terms of the action-angle variables and we also assume that, initially, the variance matrix is diagonal, i.e.,  $\sigma_{w,0} = [\sigma_{ii}\delta_{ij}]$ . With the time evolution operator,  $\Theta(t)$ , known, we can compute the variance matrix at any given time  $t$  as  $\sigma_w(t) = \Theta(t)^\dagger \sigma_{w,0} \Theta(t)$ . Equation (4) shows  $\Theta(t)$  for the 3-D case, but we reduce the equation for our purposes to the 2-D case.

After evolving the system in the action-angle space we need to transform back locally to configuration and momenta space  $\hat{\omega} = (\mathbf{x}, \mathbf{p})$  using the transformation matrix  $\mathbf{T}^{-1}$ . The elements of this matrix are related to the second derivatives of the characteristic function  $W(\mathbf{q}, \mathbf{J})$ . In our case

$$\mathbf{T}^{-1} = \begin{bmatrix} 1 & t_{12} & t_{13} & t_{14} \\ 0 & t_{22} & t_{23} & t_{24} \\ 0 & 0 & 1 & 0 \\ 0 & t_{42} & t_{43} & t_{44} \end{bmatrix}, \quad (\text{A2})$$

with

$$\begin{aligned} t_{12} &= -\frac{h(r)}{\Omega_r} W_{34} + \frac{\kappa}{p_r}, & t_{13} &= W_{33} + W_{34}t_{43}, & t_{14} &= W_{34}t_{44}, \\ t_{22} &= -\frac{h(r)}{\Omega_r} W_{44} + \frac{\Omega_r}{p_r}, & t_{23} &= W_{34} + W_{44}t_{43}, & t_{24} &= W_{44}t_{44}, \\ t_{42} &= -\frac{h(r)}{\Omega_r}, & t_{43} &= -\frac{\kappa}{\Omega_r}, & t_{44} &= \frac{p_r}{\Omega_r}, \end{aligned}$$

where

$$h(r) = -\Phi'(r) + \frac{L^2}{r^3}, \quad p_r = \sqrt{2[E - \Phi(r)] - \frac{L^2}{r^2}}, \quad \kappa = \Omega_\psi - \frac{L}{r^2},$$

and

$$W_{33} = \frac{\partial^2 W}{\partial L^2} = \int_{r_1}^r \frac{dr}{p_r} \left( \frac{\partial \Omega_\psi}{\partial J_\psi} - \frac{1}{r^2} - \frac{\kappa^2}{p_r^2} \right),$$

$$W_{44} = \frac{\partial^2 W}{\partial J_r^2} = \int_{r_1}^r \frac{dr}{p_r} \left( \frac{\partial \Omega_r}{\partial J_r} - \frac{\Omega_r^2}{p_r^2} \right),$$

$$W_{34} = \frac{\partial^2 W}{\partial L \partial J_r} = \int_{r_1}^r \frac{dr}{p_r} \left( \frac{\partial \Omega_\psi}{\partial J_r} - \frac{\kappa}{p_r^2} \Omega_r \right).$$

Subindices 1 and 3 in the expressions above refer to directions associated with  $\psi$ , such as,  $\phi_\psi$  and  $J_\psi$  whereas 2 and 4 are related to  $r$ . For more details about this procedure we refer the reader to HW.

Given  $\mathbf{T}^{-1}$ , the variance matrix at time  $t$  is expressed as:

$$\sigma_{\hat{\omega}}(t) = (\Theta(t)\mathbf{T}^{-1})^\dagger \sigma_w^0 (\Theta(t)\mathbf{T}^{-1}). \quad (\text{A3})$$

where the elements  $t_{ij}$  are evaluated at  $\langle \mathbf{x}(t) \rangle$ . Substituting  $\mathbf{T}^{-1}$ ,  $\Theta(t)$  and  $\sigma_w^0$  in the above expression, then

$$\sigma_{\hat{\omega}}(t) = \begin{bmatrix} \sigma_{11} & \sigma_{11}A & \sigma_{11}B & \sigma_{11}C \\ \{1, 2\} & \sigma_{11}A^2 + \sigma_{22}D^2 + \sigma_{44}t_{42}^2 & \sigma_{11}AB + \sigma_{22}DE + \sigma_{44}t_{42}t_{43} & \sigma_{11}AC + \sigma_{22}DF + \sigma_{44}t_{42}t_{44} \\ \{1, 3\} & \{2, 3\} & \sigma_{11}B^2 + \sigma_{22}E^2 + \sigma_{33} + \sigma_{44}t_{43}^2 & \sigma_{11}BC + \sigma_{22}EF + \sigma_{44}t_{43}t_{44} \\ \{1, 4\} & \{2, 4\} & \{3, 4\} & \sigma_{11}C^2 + \sigma_{22}F^2 + \sigma_{44}t_{44}^2 \end{bmatrix}, \quad (\text{A4})$$

where

$$\begin{aligned}
 A &= t_{12} - \Omega'_{34} t_{42} t, & B &= t_{13} - (\Omega'_{33} - \Omega'_{34} t_{43}) t, & C &= t_{14} - \Omega'_{34} t_{44} t, \\
 D &= t_{22} - \Omega'_{44} t_{42} t, & E &= t_{23} - (\Omega'_{34} - \Omega'_{44} t_{43}) t, & F &= t_{24} - \Omega'_{44} t_{44} t.
 \end{aligned}$$

In general, one is more interested in the properties of the debris in velocity space, rather than in momenta space. Therefore we transform the variance matrix according to  $\sigma_{\varpi}(t) = \mathbf{T}_{p \rightarrow v}^\dagger \sigma_{\dot{\omega}}(t) \mathbf{T}_{p \rightarrow v}$ , with

$$\mathbf{T}_{p \rightarrow v} = \begin{bmatrix} 1 & 0 & 0 & 0 \\ 0 & 1 & 0 & 0 \\ 0 & v_\psi & r & 0 \\ 0 & 0 & 0 & 1 \end{bmatrix}.$$

To obtain an expression for the time evolution of the velocity dispersions we focus our attention on what happens around a particular point  $\langle \mathbf{x}(t) \rangle$  in configuration space located on the mean orbit of the system. This is equivalent to studying the velocity submatrix of the variance matrix  $\sigma_{\varpi}(t)$ , that is

$$\sigma_{\mathbf{v}} = \begin{bmatrix} r^2(\sigma_{11}B^2 + \sigma_{22}E^2 + \sigma_{33} + \sigma_{44}t_{43}^2) & r(\sigma_{11}BC + \sigma_{22}EF + \sigma_{44}t_{43}) \\ \{1, 2\} & \sigma_{11}C^2 + \sigma_{22}F^2 + \sigma_{44}t_{44}^2 \end{bmatrix}. \quad (\text{A5})$$

By diagonalizing the matrix  $\sigma_{\mathbf{v}}$  we obtain the principal axes of the velocity ellipsoid at the point  $\langle \mathbf{x}(t) \rangle$ , and the associated dispersions. The eigenvalues of  $\sigma_{\mathbf{v}}$  are the roots of the characteristic equation:  $\det[\sigma_{\mathbf{v}} - \lambda \mathcal{I}] = 0$ . An interesting quantity is for example,  $\lambda_{v_1} \lambda_{v_2}$  because it is inversely proportional to the density:  $\rho \propto \sigma_{v_1} \sigma_{v_2} = (\lambda_{v_1} \lambda_{v_2})^{-1/2}$ . In our case:

$$\lambda_{v_1} \lambda_{v_2} = \frac{r^2 p_r^2}{\Omega_r^2} (\alpha_4 t^4 + \alpha_3 t^3 + \alpha_2 t^2 + \alpha_1 t + \alpha_0), \quad (\text{A6})$$

where

$$\begin{aligned}
 \alpha_4 &= \sigma_{11} \sigma_{22} (\det \boldsymbol{\Omega}')^2, \\
 \alpha_3 &= 2\sigma_{11} \sigma_{22} \det \boldsymbol{\Omega}' (2W_{34} \Omega'_{34} - W_{33} \Omega'_{44} - W_{44} \Omega'_{33}), \\
 \alpha_2 &= \sigma_{11} \sigma_{22} (2 \det \boldsymbol{\Omega}' \det \mathbf{W} + (\Omega'_{44} W_{33} + \Omega'_{33} W_{44})^2 + 4W_{34} (\Omega'^2_{34} W_{34} - \Omega'_{33} \Omega'_{34} W_{44} - \Omega'_{34} \Omega'_{44} W_{33})) + \\
 &\quad (\sigma_{11} \sigma_{33} + \sigma_{22} \sigma_{44}) \Omega'^2_{34} + \sigma_{11} \sigma_{44} \Omega'^2_{33} + \sigma_{22} \sigma_{33} \Omega'^2_{44}, \\
 \alpha_1 &= 2(\sigma_{11} \sigma_{22} \det \mathbf{W} (2\Omega'_{34} W_{34} - \Omega'_{44} W_{33} - \Omega'_{33} W_{44}) - \Omega'_{34} W_{34} (\sigma_{11} \sigma_{33} + \sigma_{22} \sigma_{44}) - \sigma_{11} \sigma_{44} \Omega'_{33} W_{33} - \\
 &\quad \sigma_{22} \sigma_{33} \Omega'_{44} W_{44}), \\
 \alpha_0 &= (\sigma_{11} \sigma_{22}) (\det \mathbf{W})^2 + W_{34}^2 (\sigma_{11} \sigma_{33} + \sigma_{22} \sigma_{44}) + \sigma_{11} \sigma_{44} W_{33}^2 + \sigma_{22} \sigma_{33} W_{44}^2 + \sigma_{33} \sigma_{44},
 \end{aligned} \quad (\text{A7})$$

with

$$\det \mathbf{W} = W_{33} W_{44} - W_{34}^2.$$

These equations explicitly show the behaviour of principal axes velocity dispersions:

- For very short timescales, the term with  $\alpha_0$  dominates. In this case the behaviour purely reflects the geometry of the orbit in phase space (being heavily weighted by  $r^2 p_r^2$ ).
- The terms with  $\alpha_2$  and  $\alpha_4$  are always positive, implying that these will induce a rapid increase in the  $\lambda_v$ , or a rapid decrease of the velocity dispersions on intermediate timescales.
- The terms with  $\alpha_1$  and  $\alpha_3$  can either be positive or negative, depending on location along the orbit (i.e. the  $W_{ij}$  vary in magnitude and sign). This explains the strong oscillatory behaviour observed in Fig. 3.
- On longer timescales, only the term  $\alpha_4 t^4$  is important. This gives rise to the secular behaviour of density which decreases as  $1/t^2$ , and the velocity dispersions to behave as  $1/t$  for long timescales.

To obtain the expression for the time evolution of the dispersions in configuration space we integrate the distribution function with respect to all velocities (see Eq. 8). In practice, we first transform  $\sigma_{\varpi}(t)$  from polar to Cartesian coordinates,  $\sigma'_{\varpi}(t) = (\mathbf{T}')^\dagger \sigma_{\varpi}(t) \mathbf{T}'$ , where

$$\mathbf{T}' = \begin{bmatrix} -\frac{\sin(\psi)}{r} & \frac{\cos(\psi)}{r} & 0 & 0 \\ \frac{\cos(\psi)}{r} & \frac{\sin(\psi)}{r} & 0 & 0 \\ \frac{\sin(\psi) p_r}{r} & -\frac{\cos(\psi) p_r}{r} & -\sin(\psi) & \cos(\psi) \\ -\frac{\sin(\psi) v_\psi}{r} & \frac{\cos(\psi) v_\psi}{r} & \cos(\psi) & \sin(\psi) \end{bmatrix}. \quad (\text{A8})$$

We express  $\sigma'_{\varpi}$  as

$$\sigma'_w = \begin{pmatrix} \mathbf{A} & \mathbf{B} \\ \mathbf{B}^\dagger & \mathbf{C} \end{pmatrix},$$

where the 2x2 matrices  $\mathbf{A}$ ,  $\mathbf{C}$  and  $\mathbf{B}$  represent the position submatrix, the velocity submatrix, and the cross correlation between positions and velocities, respectively (as in Eq. 2). Then, the matrix  $\sigma_{\mathbf{x}}$  is obtained from the integration of the distribution function over the velocities:

$$\sigma_{\mathbf{x}} = \begin{pmatrix} s_{11} & s_{12} \\ s_{12} & s_{22} \end{pmatrix},$$

where the elements  $s_{ij}$  are related to the dispersions in configuration space. These elements can be expressed as:

$$s_{ij} = \frac{\det \mathbf{\Gamma}_{ij}}{\det \mathbf{C}}, \quad (\text{A9})$$

with

$$\mathbf{\Gamma}_{ij} = \begin{pmatrix} a_{ij} & b_{i1} & b_{i2} \\ b_{j1} & c_{11} & c_{12} \\ b_{j2} & c_{12} & c_{22} \end{pmatrix},$$

where  $a_{ij}$ ,  $b_{ij}$  and  $c_{ij}$  are elements of the matrices  $\mathbf{A}$ ,  $\mathbf{B}$  and  $\mathbf{C}$  respectively. The diagonalization of the matrix  $\sigma_{\mathbf{x}}$  yields the values of the dispersions along the principal axes of the system in configuration space since  $\sigma_{x_i} = 1/\sqrt{\lambda_{r_i}}$ , where  $\lambda_{r_i}$  are the eigenvalues of  $\sigma_{\mathbf{x}}$ .

Solving the characteristic equation for  $\sigma_{\mathbf{x}}$  we finally obtain:

$$\lambda_{r_i} = (2\lambda_{v_1}\lambda_{v_2})^{-1} \left[ \beta_2 t^2 + \beta_1 t + \beta_0 \pm \sqrt{(\beta_2 t^2 + \beta_1 t + \beta_0)^2 - 4\lambda_{v_1}\lambda_{v_2} \det \sigma_w^0} \right], \quad (\text{A10})$$

where

$$\begin{aligned} \beta_2 &= \sigma_{11}\sigma_{22}r^2 [(\sigma_{44}\Omega'_{34} + \sigma_{33}\Omega'^2_{44})(p_r^2 + r^2\kappa^2) - 2\Omega'_{34}(\sigma_{44}\Omega'_{33} + \sigma_{33}\Omega'_{44})r^2\kappa\Omega_r + (\sigma_{44}\Omega'^2_{33} + \sigma_{33}\Omega'^2_{34})r^2\Omega_r^2], \\ \beta_1 &= -2\sigma_{11}\sigma_{22}r^2 [(\sigma_{44}W_{34}\Omega'_{34} + \sigma_{33}W_{44}\Omega'_{44})(p_r^2 + r^2\kappa^2) + ((\sigma_{33}W_{44} + \sigma_{44}W_{33})\Omega'_{34} + W_{34}(\sigma_{44}\Omega'_{33} + \sigma_{33}\Omega'_{44}))r^2\kappa\Omega_r \\ &\quad - (\sigma_{44}W_{33}\Omega'_{33} + \sigma_{33}W_{34}\Omega'_{34})r^2\Omega_r^2], \\ \beta_0 &= r^2 [\sigma_{11}(\sigma_{22}\sigma_{33}W_{44}^2 + \sigma_{44}(\sigma_{22}W_{34}^2 + \sigma_{33})) (p_r^2 + r^2\kappa^2) - 2\sigma_{11}\sigma_{22}W_{34}(\sigma_{33}W_{44} + \sigma_{44}W_{33})r^2\kappa\Omega_r + \\ &\quad \sigma_{22}(\sigma_{11}\sigma_{33}W_{34}^2 + \sigma_{44}(\sigma_{11}W_{33}^2 + \sigma_{33}))r^2\Omega_r^2]. \end{aligned} \quad (\text{A11})$$

Finally, multiplying both eigenvalues:

$$\lambda_{r_1}\lambda_{r_2} = \frac{\det \sigma_w^0}{\lambda_{v_1}\lambda_{v_2}}. \quad (\text{A12})$$